

High-Luminosity meV-Resolution Single-Shot Hard X-ray Spectrograph for Cavity-Based X-ray Free-Electron Lasers

Keshab Kauchha,¹ Peifan Liu,¹ Paresh Pradhahn,¹ and Yuri Shvyd'ko^{1,*}

¹Argonne National Laboratory, Lemont, Illinois, USA

Cavity-based x-ray free-electron lasers (CBXFELs) represent a possible realization of fully coherent hard x-ray sources having high spectral brilliance along with a narrow spectral bandwidth of $\simeq 1 - 50$ meV, a high repetition pulse rate of $\simeq 1$ MHz, and good stability. A diagnostic tool is required to measure CBXFEL spectra with meV resolution and high luminosity on a shot-to-shot basis. We have designed a high-luminosity single-shot hard x-ray spectrograph that images 9.831-keV x-rays in a $\simeq 200$ meV spectral window with a spectral resolution of a few meV. The spectrograph is designed around angular dispersion of x-rays in Bragg diffraction from crystals. It operates close to design specifications, exhibiting a linear dispersion rate of $\simeq 1.4 \mu\text{m}/\text{meV}$ and a $\simeq 200$ -meV window of high-fidelity spectral imaging. The experimentally demonstrated spectral resolution is $\simeq 20$ meV; this resolution is twice as low as expected from theory primarily because the spectrograph is highly sensitive to crystal angular instabilities. The experiment was performed at the bending magnet x-ray optics testing beamline 1-BM at the Advanced Photon Source.

I. INTRODUCTION AND PRINCIPLES OF SPECTROGRAPHS

With the advent of high-gain, single-pass x-ray free-electron lasers (XFELs) [1–4] exhibiting extreme brightness, transverse coherence, and ultra-short pulse length, a broad range of new scientific applications became possible, extending from investigation of femtosecond dynamics of atomic and molecular systems [5, 6] to detection of long-lived ultra-narrow nuclear resonances [7].

Initially, XFELs were based on a self-amplified spontaneous emission [8, 9] (SASE) process starting from shot noise and therefore having poor longitudinal coherence of x-ray pulses. Over time, various approaches have been used to improve the longitudinal coherence. Among them have been various self-seeding schemes [10–16]. A somewhat different strategy is the cavity-based x-ray free-electron laser (CBXFEL), which improves coherence by using x-ray feedback from a narrow-band x-ray cavity, such as a low-gain x-ray FEL oscillator (XFEL) [17–19] or a high-gain x-ray regenerative amplifier FEL (XRAFEL) [20–23]. This strategy holds promise for producing high-brilliance x-rays not only with full coherence and a high repetition rate of $\simeq 1$ MHz but also with good stability. The CBXFEL pulses are expected to have a narrow energy bandwidth, which can be as small as a few meV for XFELs, although with about 10^2 times smaller pulse energy of $\simeq 10 \mu\text{J}$ [17–19].

To determine the performance of a source having such a narrow bandwidth, a new diagnostic tool is required — a spectrograph capable of imaging photon spectra in a single measurement. This spectrograph will measure CBXFEL spectra with meV resolution and high luminosity on a shot-to-shot basis.

Spectrographs have been designed [24, 25] and demon-

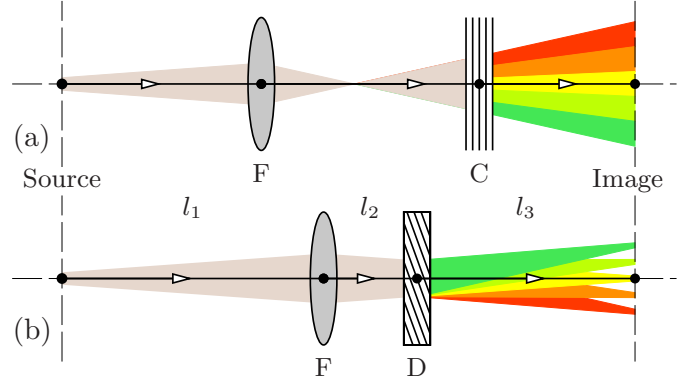


FIG. 1: Schematics of spectrographs for imaging photon spectra from x-ray sources in a single shot. (a) Spectral filter spectrograph with Bragg reflecting crystal C and focusing element F. (b) Angular dispersive spectrograph with dispersing element D — a Bragg reflecting crystal with reflecting atomic planes at a nonzero angle to the crystal surface — and focusing element F.

strated [24–27] and are in use as hard x-ray spectral diagnostic tools [25, 28] for the current generation of high-gain, single-pass XFELs [1, 2, 4, 13–16]. These devices use x-ray Bragg diffraction from crystals; namely, they exploit the fact that when diffraction occurs at particular incidence angle θ (Bragg’s angle), x-rays of a specific energy are filtered out (reflected). That is, for photon incidence at Bragg’s angle θ to reflecting atomic planes with interplanar distance d_H , exclusively x-rays of specific photon energy $E = E_H / \sin \theta$ (Bragg’s law) are reflected, where $E_H = hc/2d_H$. Figure 1(a) shows a schematic of such a “spectral filter” spectrograph. Despite a very small angular divergence ($\simeq \mu\text{rad}$) of the XFEL beams, these devices can have a significant spectral window of imaging of $\Delta E_U \simeq E\Omega / \tan \theta \simeq 50$ eV. This large spectral window is a consequence of artificially introducing a large variation ($\Omega \simeq 1$ mrad) in the incidence angle θ ei-

*Electronic address: shvydko@anl.gov

ther by focusing x-rays on the crystal [24] or by bending the crystal [25]. The energy resolution of such spectrographs is limited by the Bragg reflection bandwidth ΔE , which is typically $\simeq 1 - 0.1$ eV. The corresponding small angular acceptance ($\Delta\theta = (\Delta E/E) \tan\theta \simeq 1 - 10$ μrad) results in low luminosity ($\propto \Delta\theta/\Omega \simeq 10^{-3} - 10^{-2}$).

Spectrographs for CBXFELs must have a better spectral resolution and higher luminosity than available from current spectral filter spectrographs in use at XFELs. To this end, we apply here an alternative spectrographic approach that uses angular dispersion of x-rays in Bragg diffraction from a crystal [29, 30] — a hard x-ray grating effect — combined with focusing [31, 32].

The operating principle and basic components of the angular dispersive spectrograph are presented schematically in Fig. 1(b). Dispersing element D is a broadband Bragg crystal reflector in asymmetric scattering geometry with reflecting atomic planes at nonzero (asymmetry) angle η to the crystal surface. This dispersing element reflects x-rays of different photon energies E at different angles θ' with the angular dispersion rate $\mathcal{D} = d\theta'/dE$ similar to a diffraction grating (the angular dispersion effect). Finally, focusing element F focuses different spectral components on different locations on the image plane, located at distance l_3 from the dispersing element. In the general case, the dispersing element can be composed of several crystals (as in the present paper) exhibiting a cumulative dispersion rate \mathcal{D}_U larger than that of a single reflector [33]. Unlike the spectral filtering spectrographs in Fig. 1(a), all photons from the source are captured (within the spectral or angular acceptance ranges of the optics), thus ensuring high luminosity. In addition, the spectral resolution

$$\Delta\varepsilon = \frac{\Delta y}{|G|}, \quad G = \mathcal{D}_U l_3 \quad (1)$$

relies on the magnitude of the linear dispersion rate $G = dy/dE$ in the image plane and on the tightness of the monochromatic focal spot size Δy (see [32], Appendix, and Eq. (A10)) rather than on the smallness of the Bragg reflection bandwidth.

A proof-of-principle angular dispersive hard x-ray spectrograph was demonstrated in [33], where it was also shown that multiple crystal arrangements can enhance the cumulative angular dispersion rate of the system \mathcal{D}_U , which is critical for achieving high spectral resolution (Eq. (1)). Practical spectrographs were demonstrated for applications in nuclear resonance [34] and resonant inelastic scattering (RIXS) [35] spectroscopies.

The spectrograph presented in this publication was designed to characterize x-ray pulses of a CBXFEL demonstrator [36–38], which is being developed through a joint project of Argonne National Laboratory, SLAC National Accelerator Laboratory, and RIKEN. The CBXFEL will be driven by electron beams of the Linac Coherent Light Source (LCLS) facility at SLAC [1] and operated at a fixed nominal photon energy of $E = 9.831$ keV to produce x-ray pulses with a bandwidth of $\lesssim 60$ meV. These

Parameter(s)	Notation or expression	Value	
		1BM	LCLS
X-ray source			
Size (FWHM) [μm]	$\Delta x/\Delta y$	198/78	60/60
Photon energy [keV]	E	9.831 keV	
Dispersing element D and crystals C_1, C_2			
Bragg angles	$\theta_1 = \theta_2$	18.38°	
Asymmetry angles	$\eta_1 = -\eta_2$	−16.4°	
Angular acceptance [μrad]	$\Delta\theta_1, \Delta\theta_2$	196, 12	
Asymmetry factors	b_1, b_2 (A1)	−0.061, −16.5	
Cumulative factor	$b_U = b_1 b_2$ (A14)	1	
Angular dispersion rates [$\mu\text{rad}/\text{meV}$]	$\mathcal{D}_1, \mathcal{D}_2$ (A1)	−0.032, +0.52	
Cumulative dispersion rate [$\mu\text{rad}/\text{meV}$]	$\mathcal{D}_U = \mathcal{D}_1 b_2 + \mathcal{D}_2$ (A14)	1.05	
Spectral window of imaging [meV]	ΔE_U	198	
Focusing element F (CRL) and lenses			
Be-lens radius [μm]	R	200	
Number of lenses	N_L	16	
Focal length [m]	$f = R/(2N_L \delta^a)$ [40]	1.772	
Spectrograph			
Distances between elements [m]	l_1	$\simeq 35.1$	$\simeq 250$
	l_3, d_{12}	1.39,	0.15
De-magnification	$\tilde{l}_{23} = f l_1 / (l_1 - f)$	1.87	1.78
	$l_2 = \tilde{l}_{23} - l_3$ (A18)	0.48	0.39
Mono. image size [μm]	$A = -\tilde{l}_{23}/l_1$ (A17)	0.053	0.007
Linear dispersion rate [$\mu\text{m}/\text{meV}$]	$\Delta x'/\Delta y'$	10.5/4.1	
Spectral resolution	$G_U = \mathcal{D}_U l_3$	1.46	
−Ultimate [meV]	$\Delta\varepsilon$	2.2	0.24
−Expected [meV]	$= \Delta y / (l_1 \mathcal{D}_U)$	8.3 ^b	
	$= \Delta y'_e / G_U$		

^aRefractive index $n = 1 - \delta$, where decrement $\delta = 3.52 \times 10^{-6}$ in Be.

^bHere, the actual monochromatic focal spot size $\Delta y'_e = 12$ μm is used to calculate the expected resolution; see Fig. 3(a).

TABLE I: Design parameters of x-ray sources (1-BM at APS or LCLS at SLAC); dispersing element D; focusing element F; and spectrograph.

parameters determine the design values of the spectrograph: photon energy E , spectral window of imaging $\Delta E_U \gtrsim 100$ meV, and spectral resolution $\Delta\varepsilon \simeq 10$ meV. In the following discussion, we present design details of the spectrograph and results of tests performed at x-ray optics beamline 1-BM at the Advanced Photon Source (APS) at Argonne National Laboratory [39].

II. OPTICAL DESIGN AND COMPONENTS OF THE SPECTROGRAPH

To achieve the needed spectral resolution of $\Delta\varepsilon \simeq 10$ meV, a dispersing element D with an angular dispersion rate of $\mathcal{D} \simeq 1$ $\mu\text{rad}/\text{meV}$ is required (see Eq. (1)),

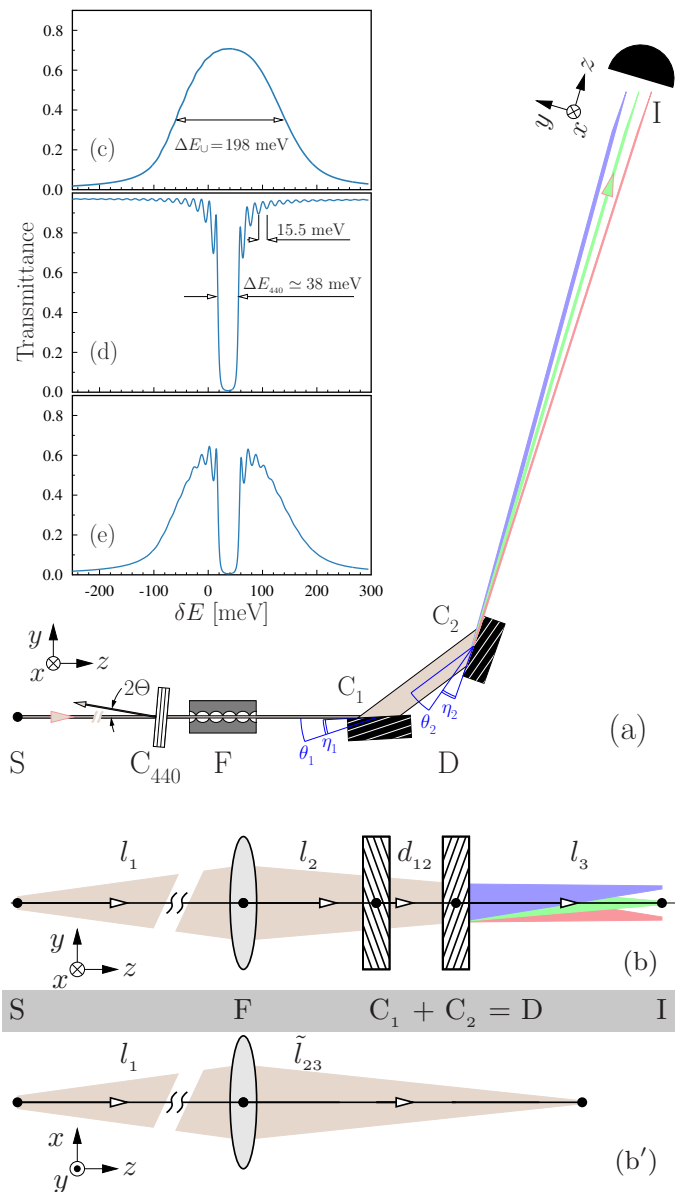


FIG. 2: Schematics and spectral profiles of the angular dispersive spectrograph. (a) Optical scheme shown in the diffraction (y, z) plane with x-ray source S, focusing element F, double-crystal dispersing element D composed of crystals C_1 - C_2 , and x-ray imager I. Crystal C_{440} is a spectral resolution probe; see part (d). (b)-(b') Equivalent unfolded optical schemes in the diffraction (b) and (x, z) sagittal (b') planes. (c)-(e) Spectral profiles of x-rays passing through (c) crystals C_1 - C_2 ; (d) a spectral resolution probe — a narrow-band diamond Bragg back-reflecting crystal C_{440} ; and (e) through both C_{440} and C_1 - C_2 . See text for details.

assuming $\Delta y \simeq 10 \mu\text{m}$ and $l_3 \simeq 1$ m. This performance can be realized by using a rather simple dispersing element D composed of two asymmetrically cut crystals C_1 and C_2 in the mirror-symmetric dispersive ($++$) arrangement, as shown in the optical scheme of the spectrograph in Fig. 2(a). The spectrograph is shown in the diffraction

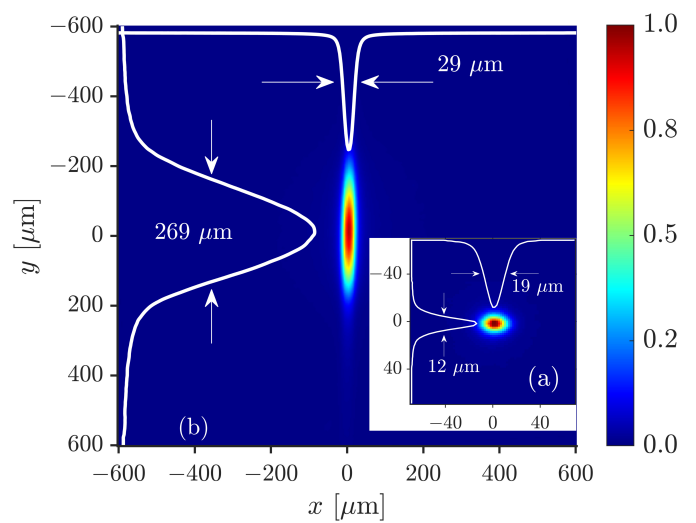


FIG. 3: Images of the monochromatized x-ray beam from a bending magnet source take in (a, inset) inline focusing configuration S-F-I of Fig. 2(b'), and (b) in spectrograph configuration S-F- C_1 - C_2 -I of Figs. 2(a)-(b) with the double-crystal element D (C_1 - C_2) dispersing x-rays in the diffraction plane (y -direction). Also shown are beam profiles $S(y)$ and $S(x)$, which are a result of integrating the images over x and y , respectively.

plane (y, z), which coincides with the angular dispersion plane.

To achieve the target value of the cumulative dispersion rate \mathcal{D}_U , the low-index 220 Bragg reflections from Ge crystals are used, with the parameters provided in Table I. The use of Ge, rather than the more standard Si, makes it possible to maximize the spectral window of imaging to $\Delta E_U = 198$ meV and the angular acceptance. The calculated spectral profile of the x-rays reflected by the crystals¹ is shown in Fig. 2(c). The crystals were manufactured at the APS. Dispersing elements in the same configuration were used previously in [34, 35]. This is the simplest configuration that ensures enhancement of the cumulative rate \mathcal{D}_U vs. dispersion rate of a single reflector. Simultaneously, it leaves unchanged the beam cross-section at the exit of the dispersing element, as the cumulative asymmetry factor b_U is 1 in this case.

The focusing element F is a compound refractive lens (CRL) [41] composed of paraboloidal beryllium lenses [40] with parameters presented in Table I.

The spectrograph design parameters also shown in Table I are optimized using the equations of the spectrograph theory [32] that are presented in a focused form in Appendix A. We also show there that the nonzero distance d_{12} between crystals C_1 and C_2 of the dispersing

¹ The calculations are performed for x-rays with a 100- μrad divergence introduced by focusing lens F, which is smaller than the angular acceptance of the dispersing element.

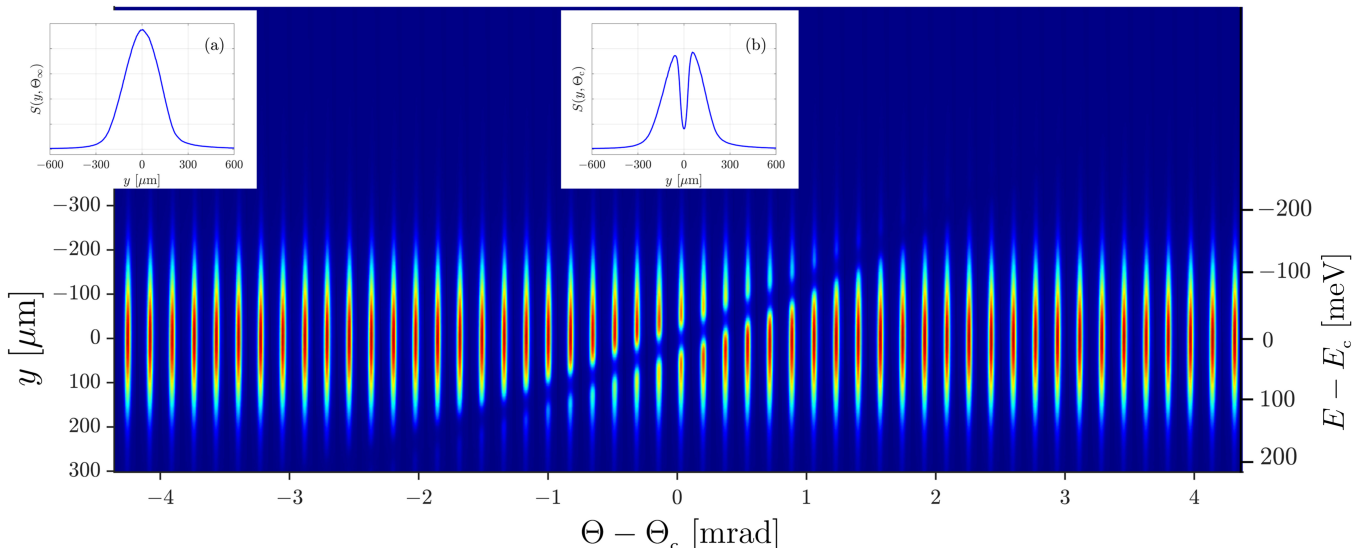


FIG. 4: A sequence of x-ray spectrograph images similar to that in Fig. 3(b) but taken here with spectral resolution probe C_{440} in the beam and angular deviation Θ from the exact Bragg back reflection being changed incrementally. Inserts show examples of spectral profiles $S(y, \Theta)$ taken at selected angles $\Theta_\infty = 4.91$ mrad (inset a) and $\Theta_c = 9.26$ mrad (inset b). The Θ scale is centered at $\Theta_c = 9.259$ mrad; this value corresponds to the notch in the middle of the spectral window of imaging (inset b). The energy scale $E - E_c = G^{(\text{exp})}y$ is obtained using the linear dispersion rate $G^{(\text{exp})}$ derived from these images as detailed in the discussion of Fig. 5.

element leads to astigmatism: the focal points of x-rays propagating in the mutually perpendicular (y, z) diffraction and (x, z) sagittal planes are spaced by $\simeq d_{12}$ along the optical axes, as illustrated on the equivalent unfolded schemes of the spectrograph in Figs. 2(b) and (b').

To characterize the spectrograph's performance — dispersion rates, spectral resolution, spectral window of imaging — a spectral resolution probe C_{440} is added to the setup, as shown in Fig. 2(a). Crystal C_{440} is an x-ray-transparent diamond crystal of thickness $d = 40 \mu\text{m}$ in the 440 Bragg reflection close to backscattering with incidence angle $\Theta \ll 1$. Inserting this crystal creates an absorption notch in the x-ray transmission spectrum having a bandwidth $\Delta E_{440} = 38$ meV of the Bragg reflection. The tails of the notch display fringes of equal thickness with a periodicity of $hc/2d = 15.5$ meV. The calculated spectrum is shown in Fig. 2(d). Figure 2(e) presents the result of the combined action of C_1 - C_2 and C_{440} on the spectrum of x-rays propagating through the system. The energy variation of the absorption notch location, $\delta E/E = \tan \Theta \delta \Theta$, is controlled by variation of the incidence angle $\delta \Theta$ according to Bragg's law; this relationship enables energy calibration of the spectrograph. The backscattering geometry ensures that the spectral profile of the notch is insensitive to the angular divergence of the x-ray beam and also permits straightforward measurement of Θ .

In the experiment, a double-crystal Si(111) monochromator is used upstream of C_{440} to reduce the bandwidth of x-rays to about 1 eV [39]. This monochromator is not shown in Fig. 2(a). The spectral flux density of photons

provided to the experiment is $\simeq 10^9$ ph/s/eV/mm².

III. EXPERIMENT

In the first measurement, the monochromatic x-ray source image size was determined to assess the energy resolution that can be achieved under the given experimental conditions of beamline 1-BM [39] at APS. Figure 3(a) shows the source image with a full width at half maximum (FWHM) of $\Delta x'_e \times \Delta y'_e = 19 \times 12 \mu\text{m}^2$. It was measured in the inline S-F-I configuration excluding the dispersing element as in the equivalent scheme of Fig. 2(b'), with l_1 and \tilde{l}_{23} values from Table I. Given the 1-eV bandwidth of the x-rays, focusing by the CRL can be considered achromatic, and therefore the measured sizes correspond to the monochromatic source image size. Both horizontal and vertical values, and especially the vertical [see Fig. 3(a)], are larger than the design monochromatic image size $\Delta x' \times \Delta y'$ given in Table I. This broadening occurs mostly because of imperfections in the upstream beamline optical components, e.g., the Si(111) monochromator and Be windows, and the limited spatial resolution $\simeq 6 \mu\text{m}$ of the YaG:Ce-based scintillator x-ray imager. The imager uses a low-noise Andor Zyla 4.2 Plus camera and Infinity KC VideoMax optic with IF-3.5 objective [37]. The vertical size determines the smallest spectral resolution that can be expected under conditions of the present experiment: $\Delta \varepsilon_e \simeq 8$ meV (see Table I).

In the next step, the dispersing element was added to complete the spectrograph. Figure 3(b) demonstrates its

immediate effect: the y -image size is greatly enlarged from $12\ \mu\text{m}$ to $269\ \mu\text{m}$ (FWHM). The image was taken in the location of the diffraction plane focus, which is away from the sagittal focus by about $d_{12} = 15\ \text{cm}$ due to astigmatism in the system. (The best focusing in the diffraction and sagittal planes is determined by lens equations (A19) and (A22), respectively; see also the numerical simulations discussed in the next section.) Because of this difference in focal position, the x -image size in Fig. 3(b) is larger than that in Fig. 3(a). The pitch angles of crystals C_1 and C_2 (corresponding to θ_1 and θ_2) were aligned by maximizing the intensity of reflected x-rays, while the yaw and roll angles were aligned to minimize the x -image size of the source in the sagittal image plane, which is unaffected by the angular dispersion effect. The images were made with $\simeq 10^7$ photons (exposure time 10 s), and a signal-to-noise ratio of $\simeq 150$.

Finally, the spectral resolution probe C_{440} was added to the setup to measure the dispersion rates, the spectral resolution, and the window of imaging of the spectrograph. Figure 4 shows a sequence of x-ray spectrograph images similar to that in Fig. 3(b) but taken here with the spectral probe in the beam and the angular deviation Θ from exact Bragg back reflection being changed incrementally. As already noted, the effect of C_{440} is to produce an absorption notch. The spectral location of this notch (imager's coordinate y) varies with Θ according to Bragg's law. The Θ -scale is centered at $\Theta_c = 9.259\ \text{mrad}$; at this angle, the notch is in the middle of the spectral window of imaging of the spectrograph. Also shown are examples of spectral image profiles $S(y, \Theta)$ taken at selected angles $\Theta_\infty = 4.91\ \text{mrad}$ and $\Theta_c = 9.26\ \text{mrad}$ [Figure 4, insets (a) and (b), respectively].

Figure 5 shows an example of a normalized absorption notch profile $N(y, \Theta)$ in panel (a) and plots of normalized notch parameters in panels (b)-(d) as a function of angular deviation $\Theta - \Theta_c$ derived from the images of Fig. 4. The normalized absorption notch profile $N(y, \Theta) = S(y, \Theta)/S(y, \Theta_\infty)$ is defined as the ratio of the x-ray beam spectral image profile $S(y, \Theta)$ at a particular angle Θ [see Fig. 4(b)] to the x-ray beam image profile $S(y, \Theta_\infty)$ when unaffected by the absorption notch [see Fig. 4(a)]. Figures 5(b)-(d) present, respectively, the position y_n of the absorption notch minimum, the notch width Δy_n (FWHM), and absorption effect, all as function of $\Theta - \Theta_c$, evaluated for each normalized absorption notch profile $N(y, \Theta)$.

In Figs. 5(b) through 5(d), the bottom angular scale $\Theta - \Theta_c$ is converted into the top energy scale $E - E_c$ using Dumond tangent $D_t = dE/d\Theta|_c = E_c \tan \Theta_c = 91(5)\ \text{meV/mrad}$ derived from Bragg's law at $\Theta = \Theta_c$. The main contribution to the error of D_t is a $\simeq 0.4\ \text{mrad}$ inaccuracy in determination of Θ_c in the experiment. The red line in Fig. 5(b) is a quadratic fit. The green line is its tangent $T = dy_n/d\Theta|_c = -124\ \mu\text{m/mrad}$ at $\Theta = \Theta_c$. The spatial scales on the left of Figs. 5(b) and 5(c) and on Fig. 4 are converted to the energy scales on the right using the linear dispersion rate of the spectro-

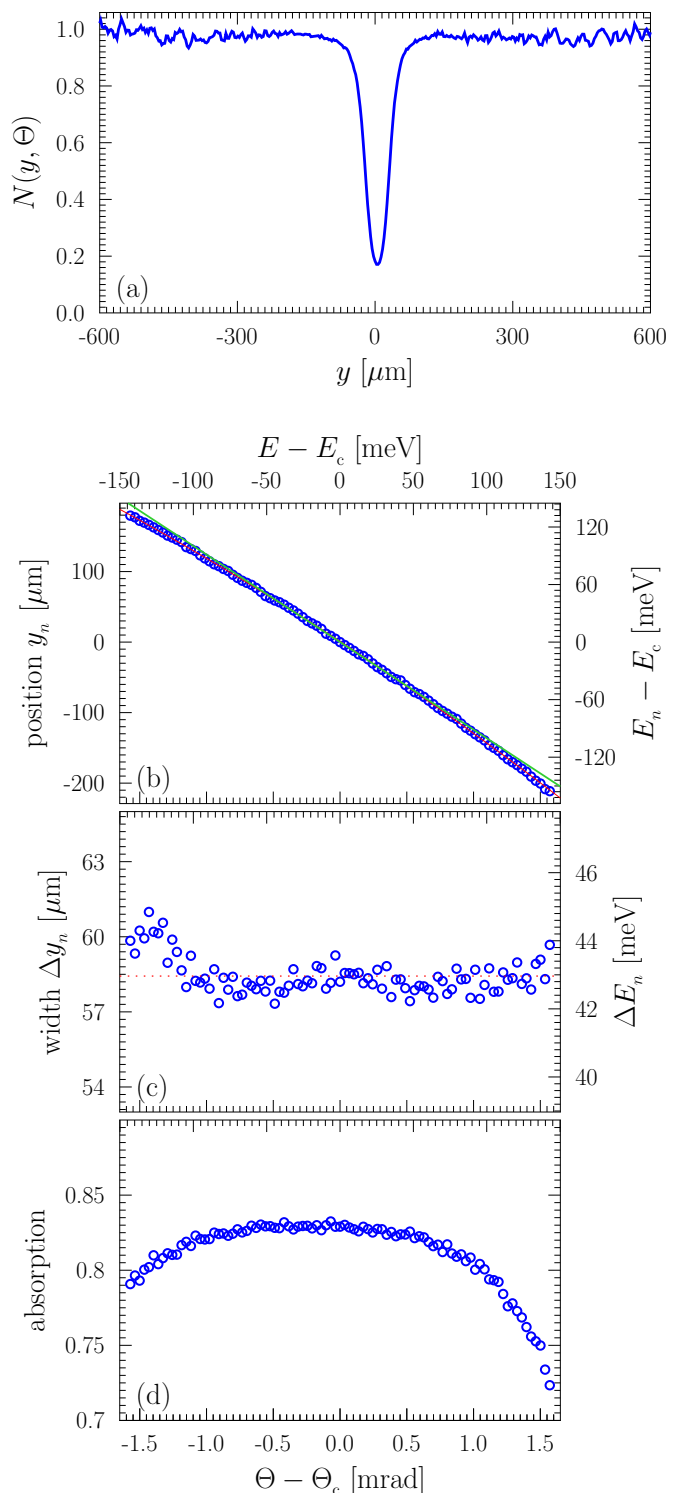


FIG. 5: Normalized absorption notch profiles $N(y, \Theta)$ and notch parameters as a function of angular deviation Θ from exact Bragg backscattering of probe C_{440} . (a) An example of the normalized absorption notch profile $N(y, \Theta) = S(y, \Theta)/S(y, \Theta_\infty)$: that is, the ratio of the x-ray beam spectral image profile $S(y, \Theta)$ [see Fig. 4(b)] to the x-ray beam image profile $S(y, \Theta_\infty)$ when unaffected by the absorption notch [see Fig. 4(a)]. (b) Absorption notch location y_n . (c) Notch full width at half maximum (FWHM) Δy_n . (d) Absorption effect.

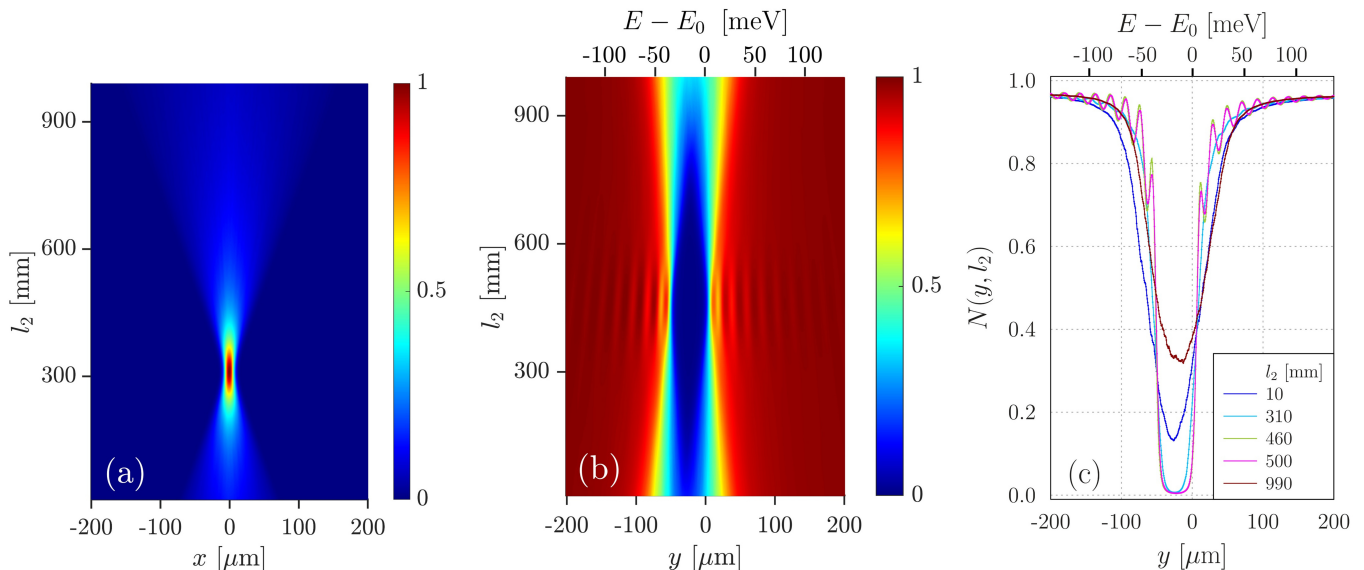


FIG. 6: Numerical simulations of x-ray imaging by the spectrograph. (a) 2D color map of the image profiles $S(x, l_2)$ in the sagittal plane as a function of distance l_2 between movable focusing element F (CRL) and fixed crystal C_1 . (b) 2D color map of the normalized absorption notch profiles $N(y, l_2)$ in the diffraction plane as a function of l_2 . (c) Examples of the normalized absorption notch profiles $N(y, l_2)$ at particular l_2 .

graph, $G^{(\text{exp})} = dy_n/dE|_c = T/D_t = 1.36(7) \mu\text{m}/\text{meV}$. The value of the linear dispersion rate $G^{(\text{exp})}$ obtained from the experimental data is in a good agreement with the design value G of Table I.

This result allows us to determine the spectral window of imaging that corresponds to the image width $\Delta y = 269 \mu\text{m}$ in Fig. 3(b), namely, $\Delta E_{\text{J}}^{(\text{exp})} = 198(10) \text{ meV}$. This value also agrees well with the design value ΔE_{J} of Table I. Importantly, this result not only present the characteristic spectral range of the x-rays transmitted through the spectrograph but also identify the region in which the normalized notch profile has a constant width and relatively constant absorption effect [see Figs. 5(c) and 5(d)], that is, the region where the spectral imaging has its highest fidelity.

Accordingly, the notch width measured by the imager, $\Delta y_n = 58.5 \mu\text{m}$ [Fig. 5(c)] can be translated to a spectral notch width of $\Delta E_n = 43(2) \text{ meV}$. The latter is close to, albeit larger than, the theoretical value of $\Delta E_{440} = 38 \text{ meV}$ of Fig. 2(d). This difference indicates the spectrograph has a limited spectral resolution, which can be estimated as $\varepsilon^{(\text{exp})} = \sqrt{(\Delta E_n)^2 - (\Delta E_{440})^2} = 20(4) \text{ meV}$. This value is more than a factor of two larger than the expected value of $\varepsilon_c = 8.3 \text{ meV}$ (Table I). It is also larger than the 15.5-meV period of the fringes seen in the theoretical spectral profiles in Figs. 2(d) and 2(e) and explains why these fringes are not observed in the experiment, e.g., in Fig. 5(a). Moreover, it is due to this limited spectral resolution that the measured absorption effect is about 83% [Fig. 5(d)] rather than the 99% expected from theory [Fig. 2(d)].

IV. NUMERICAL SIMULATIONS AND DISCUSSION

Numerical simulation results of x-ray imaging by this angular dispersive spectrograph, shown in Fig. 6, present its ultimate performance under idealized conditions of the experiment. The simulations were carried out with the x-ray optics modeling package Shadow3 [42] in the Oasys environment [43, 44] using the parameters given in Table I. The locations of the x-ray source, crystals C_1 and C_2 , and the image plane are fixed. The conditions for the best focusing in the image plane are determined from variation of distance l_2 between the focusing element F (CRL) and crystal C_1 . The results of the numerical simulations show that the best focusing for rays propagating in the sagittal and diffraction planes takes place at different locations of the focusing element. The best focusing in the sagittal plane is revealed from the sharpest image size at $l_2 \simeq 310 \text{ mm}$ on the 2D color map of image profiles $S(x, l_2)$ in Fig. 6(a). The best focusing in the diffraction plane takes place at $l_2 \simeq 480 \text{ mm}$, as reflected in the largest absorption effect and in the highest visibility of the fringes of equal thickness on the tails of the normalized absorption notch profiles $N(y, l_2)$ on the 2D color map of $N(y, l_2)$ in Fig. 6(b). Examples of the normalized absorption notch profiles $N(y, l_2)$ at particular l_2 are shown additionally in Fig. 6(c). These results are in agreement with lens equations (A19) and (A22) for focusing in the diffraction and sagittal planes, respectively, and in agreement with the results of the experiment.

The limited spectral resolution observed in the experiment — in particular, the inability of the spectrograph

to resolve fringes of equal thickness — is likely due to the following two reasons.

First, the x-ray trajectory in the (y, z) diffraction plane is sensitive to pitch angle instabilities of crystals C_1 and C_2 , resulting in blurring of the image profiles $S(y)$. As we show in Appendix B, an angular variation ϕ of the crystal pitch angle of either of the crystals results in a shift of the spectral image by $\delta y' \simeq l_3 b_2 \phi$, an effect aggravated by the large absolute value of $|b_2|$. For example, an angular error of $\phi = 1 \mu\text{rad}$ of one of the crystals, which could be caused by vibrations, for example, results in a spatial shift of $\delta y' \simeq 22 \mu\text{m}$ or in an equivalent energy shift of $\delta y'/G \simeq 16 \text{ meV}$. Such variations can blur sharp spectral features and degrade the spectral resolution. Vibrations were minimized during the experiment but were not eliminated completely.

Second, imperfect roll and yaw angular alignment of crystals C_1 and C_2 results in mutually nonparallel diffraction and dispersion planes, which also degrades the resolution. Minimizing the image size in the sagittal plane by varying the roll and yaw angles, which was used in the experiment, is a tedious and equivocal procedure. It could be improved in the future experiments by better pre-alignment of the crystals.

We note that crystal imperfections are unlikely to be the cause of the degradation in resolution compared to theory, since the x-ray rocking curve imaging topography [45–47] of crystals C_1 and C_2 revealed high crystal quality: almost theoretical values for the 440 Bragg reflection width and small Bragg plane slope variations of only $\simeq 0.1 \mu\text{rad}$ (rms) over large crystal areas of $10 \times 10 \text{ mm}^2$.

V. SUMMARY

A high-luminosity meV-resolution single-shot hard X-ray spectrograph was designed as a CBXFEL spectral diagnostic tool to image 9.831-keV x-rays in a $\simeq 200 \text{ meV}$ spectral window with a spectral resolution of a few meV. The operational principle of the spectrograph is angular dispersion of x-rays in Bragg diffraction from crystals. The spectrograph operates close to design specification, exhibiting a linear dispersion rate of $1.36 \mu\text{m}/\text{meV}$ and a 200-meV window of high-fidelity spectral imaging. The experimentally obtained spectral resolution of $\simeq 20 \text{ meV}$ is limited by high sensitivity to crystal angular instabilities at the optics testing bending magnet beamline 1-BM at the Advanced Photon Source, where it was tested.

Acknowledgments

Kwang-Je Kim, Marion White, Lahsen Assoufid (Argonne) and Clement Burns (WMU) are acknowledged for discussions and support. Xianrong Huang and Elina Kazman (Argonne) are acknowledged for manufacturing the germanium crystals for the dispersing element. Sergey

Terentev and Vladimir Blank (FSBI TISNCM) are acknowledged for manufacturing the diamond crystal for the spectral resolution probe. We are grateful to Michael Wojcik and Brandon Stone (Argonne) for supporting experiments at APS beamline 1-BM. Luca Rebuffi (Argonne) is acknowledged for helping to set up x-ray optics modeling with package Shadow3 in the Oasys environment. This research used resources of the Advanced Photon Source, a U.S. Department of Energy (DOE) Office of Science user facility at Argonne National Laboratory and is based on research supported by the U.S. DOE Office of Science—Basic Energy Sciences, under Contract No. DE-AC02-06CH11357.

Appendix A: Spectrograph theory with an account of spacing between the dispersive crystals

A theory of the x-ray angular dispersive spectrograph was introduced in [32]. The ray-transfer matrix technique was used to derive the spectral resolution and other characteristics of the spectrograph for diverse configurations of the crystal dispersing elements and the focusing and collimating optics. The same technique is applied here to the particular case of the spectrograph in the “focusing-monochromator-I” (FM1) configuration considered in the present paper, with one focusing element and the two-crystal dispersing element, as shown in the equivalent optical scheme in Fig. 2(b). The nonzero distance between the crystals is accurately taken into account, resulting in astigmatism in focusing.

1. General equations

The spectrograph in the FM1 configuration consists of the focusing element F with a focal length f at a distance l_1 from the x-ray source S and a dispersing element with N crystals C_n ($n = 1, 2, \dots, N$) in asymmetric Bragg diffraction, each characterized by the asymmetry factor b_n and angular dispersion rate $\mathcal{D}_n = d\theta'_n/dE$:

$$b_n = -\frac{\sin(\theta_n + \eta_n)}{\sin(\theta_n - \eta_n)}, \quad \mathcal{D}_n = -\frac{1 + b_n}{E} \tan \theta_n. \quad (\text{A1})$$

Here, θ and θ' are the glancing angle of incidence (Bragg’s angle) and reflection, respectively, to the diffracting atomic planes; η is the asymmetry angle — the angle between the diffracting atomic planes and the entrance crystal surface; E is the x-ray photon energy. Figure 2(a) shows an example of a spectrograph with a two-crystal dispersing element, while Figs. 2(b) and 2(b’) show equivalent unfolded schemes.

In the following, cumulative values are also used for the asymmetry parameter b_{\cup_n} and the angular dispersion rate \mathcal{D}_{\cup_n} ; these values result from successive Bragg reflection from n crystals ($1 \leq n \leq N$), which are defined

as

$$b_{\cup_n} = b_1 b_2 b_3 \dots b_n, \quad \mathcal{D}_{\cup_n} = b_n \mathcal{D}_{\cup_{n-1}} + s_n \mathcal{D}_n. \quad (\text{A2})$$

Here $s = -1$ for clockwise and $s = +1$ for counterclockwise ray deflection upon Bragg reflection.

The first crystal C_1 is at a distance l_2 from the focusing element F, and the last crystal C_N is at a distance l_3 from the image plane with position-sensitive imager I. There are nonzero distances $d_{n-1\ n}$ between crystals C_{n-1} - C_n of the dispersing element.

Following [32], x-rays of each monochromatic spectral component E emerging from the source S with a lateral size $\Delta x \times \Delta y$ are focused to $\Delta x'$ in the sagittal (x, z) plane and to $\Delta y'$ in the diffraction (y, z) plane:

$$\Delta u' = A \Delta u, \quad u = x \vee y, \quad A = \frac{1}{b_{\cup_N}} \left(1 - \frac{\tilde{l}_{23}}{f} \right), \quad (\text{A3})$$

$$\tilde{l}_{23} = l_{23} + b_{\cup_N} B_{\cup_N}, \quad l_{23} = l_2 + l_3 b_{\cup_N}^2, \quad (\text{A4})$$

$$B_{\cup_n} = \frac{B_{\cup_{n-1}} + b_{\cup_{n-1}} d_{n-1\ n}}{b_n}, \quad B_{\cup_1} = 0, \quad (\text{A5})$$

where, the relationship between f , l_1 , l_2 , $d_{n-1\ n}$, and l_3 is determined by the lens equation for the condition of best focusing:

$$\frac{1}{l_1} + \frac{1}{\tilde{l}_{23}} = \frac{1}{f}. \quad (\text{A6})$$

With this equation the magnification factor in Eq. (A3) can be presented as

$$\Delta u' = A \Delta u, \quad u = x \vee y, \quad A = -\frac{1}{b_{\cup_N}} \frac{\tilde{l}_{23}}{l_1}. \quad (\text{A7})$$

Importantly, according to Eq. (A6) the virtual lens-to-image-plane distance \tilde{l}_{23} is solely determined by l_1 , and f and is independent of the details of the design of the dispersing element.

We assume that Bragg diffraction takes place only in the diffraction (y, z) plane. However, when considering focusing of x-rays in the sagittal (x, z) plane, which are unaffected by diffraction in the plane perpendicular to it, we have to use in this case $b_n = -1$ and $\mathcal{D}_n = 0$ for all crystals. As a result, although lens equation (A6) and the virtual distance \tilde{l}_{23} for the best focusing are the same in both planes, assuming the same l_1 and f , the magnification factor [Eq. (A7)] and the image plane locations for x-rays propagating in the diffraction (y, z) and the sagittal (x, z) planes [determined by l_2 , $d_{n-1\ n}$, l_3 from Eqs. (A4)-(A5)] can differ. Therefore, generally speaking, focusing systems that contain dispersing elements exhibit astigmatism: diffraction and sagittal rays form foci at different distances along the optic axis.

A change δE in the x-ray photon energy E results in a change of the focal spot location in the diffraction (y, z) plane by

$$\delta y = G \delta E, \quad G = \mathcal{D}_{\cup_N} l_3 + G_{\cup_N}, \quad (\text{A8})$$

$$G_{\cup_n} = \frac{G_{\cup_{n-1}} + \mathcal{D}_{\cup_{n-1}} d_{n-1\ n}}{b_n}, \quad G_{\cup_1} = 0, \quad (\text{A9})$$

as a result of the angular dispersion in Bragg diffraction from the asymmetrically cut crystals. Here, G is the linear dispersion rate of the spectrograph.

An energy variation, which results in a change $|\delta y|$ of the location of the source image [Eq. (A8)] that is equal to the monochromatic source image size $\Delta y'$ [Eqs. (A3)-(A6)] determines the energy resolution of the spectrograph:

$$\Delta \varepsilon_u = \frac{\Delta y'}{|G|}. \quad (\text{A10})$$

Using Eq. (A7) for the magnification factor, the expression for the ultimate spectral resolution of the spectrograph (in the FM1 configuration) can be presented via the source y -size as follows:

$$\Delta \varepsilon_u = \frac{|\Delta y| \tilde{l}_{23}}{|G b_{\cup_N}| l_1}. \quad (\text{A11})$$

The monochromatic source image size $\Delta y'_e$ in an actual experiment can be larger than the ultimate value $\Delta y'$ given by Eq. (A7) because of imperfections in the optical elements of the spectrograph or limited imager spatial resolution. In this case, the energy resolution of the spectrograph is given by

$$\Delta \varepsilon_e = \frac{\Delta y'_e}{|G|}. \quad (\text{A12})$$

2. Two-crystal mirror-symmetric arrangement

In a particular case of the two-crystal ($N = 2$) dispersing element in mirror-symmetric dispersive ($++$) arrangement schematically presented in Fig. 2, the crystal angles are

$$\theta_1 = \theta_2, \quad \eta_1 = -\eta_2 < 0. \quad (\text{A13})$$

In this case, using Eq. (A2), the cumulative values are given by

$$b_{\cup_2} = b_1 b_2 = 1, \quad \mathcal{D}_{\cup_2} = b_2 \mathcal{D}_1 + \mathcal{D}_2. \quad (\text{A14})$$

Further, the expression for the virtual lens-to-image plane distance

$$\tilde{l}_{23} = l_2 + l_3 + b_1^2 d_{12} \quad (\text{A15})$$

is obtained from Eqs. (A4)-(A5) and $B_{U_2} = b_1 d_{12}/b_2$. Furthermore, the linear dispersion rate

$$G = \mathcal{D}_{U_2} l_3 + \frac{\mathcal{D}_1 d_{12}}{b_2}. \quad (\text{A16})$$

is obtained from Eqs. (A8)-(A9) and $G_{U_2} = \mathcal{D}_1 d_{12}/b_2$, while the expression for the magnification factor

$$A = -\frac{\tilde{l}_{23}}{l_1} \quad (\text{A17})$$

is derived from Eqs. (A7) and (A14).

If the crystal asymmetry is large, i.e., $-b_1 = -1/b_2 \ll 1$, and the distance between the crystals is small, i.e., $d_{12} \ll l_2 + l_3$ (as in our experiment), then the term $b_1^2 d_{12}$ can be omitted in Eq. (A15). The linear dispersion term $\mathcal{D}_1 d_{12}/b_2$ in Eq. (A16) can be also neglected. In this case, d_{12} does not enter the virtual lens-to-image plane distance

$$\tilde{l}_{23} \simeq l_2 + l_3, \quad (\text{A18})$$

and it appears as if distance d_{12} has no impact either on the lens equation, which now reads as

$$\frac{1}{l_1} + \frac{1}{l_2 + l_3} = \frac{1}{f}, \quad (\text{A19})$$

or on the spectral resolution

$$\Delta\varepsilon = \frac{\Delta y}{\mathcal{D}_{U_n} l_3} \frac{l_2 + l_3}{l_1}. \quad (\text{A20})$$

On the other hand, in the symmetric case when $b_1 = b_2 = -1$, the virtual lens-to-image plane distance becomes

$$\tilde{l}_{23} = l_2 + l_3 + d_{12}, \quad (\text{A21})$$

i.e., is exactly equal to the length of the optical path from the lens to the imager, with the lens equation taking the expected form

$$\frac{1}{l_1} + \frac{1}{l_2 + l_3 + d_{12}} = \frac{1}{f}. \quad (\text{A22})$$

Here we emphasize that the virtual distance \tilde{l}_{23} is an invariant. What changes is the relationship between l_2 and l_3 and thus the location of the image planes. In relation to our experiment, these results mean that there are two different image planes for focusing of the rays in the diffraction plane (y, z) and in the sagittal (x, z) plane perpendicular to it. The sagittal image plane location is defined by focusing equation (A22), while the diffraction image plane location is defined by focusing equation (A19) and is d_{12} further away from the second crystal than the sagittal image plane, as shown in the equivalent unfolded schemes in Figs. (b) and 2(b').

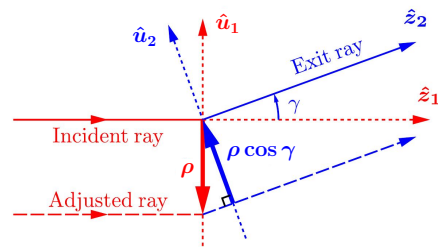


FIG. 7: Schematic of incident and adjusted rays clarifying calculation of the x-ray trajectory distorted by a misaligned optical element [49].

Appendix B: Ray trajectory distortions caused by angular errors of C_1 and C_2 crystals

In this section we study how much an angular misalignment ϕ of either crystal C_1 or C_2 of the dispersing element of the spectrograph can change the x-ray trajectory and therefore the image location in the imager plane. In practical terms, this knowledge determines tolerances on angular stability of the dispersing element crystals.

1. General equation

The ray-transfer matrix approach can be used to propagate rays through optical systems with misaligned optical elements [48, 49].

Figure 7 (adapted from [49]) illustrates the equations used to calculate misalignments. Suppose an optical element (a crystal or a lens) is displaced from the perfect configuration by a distance ρ and an angle ϕ . The distorted propagation of the x-rays can be calculated by (i) displacing the incident x-ray presented by vector \mathbf{r}_1 with spatial and angular coordinates u_1 and v_1 , respectively, by the same amount as the optical element but in the opposite direction ($-\rho$ and $-\phi$); (ii) transferring the ray with an appropriate matrix \hat{M} of the optical element; and (iii) moving the transferred ray back by the adjusted amount. As a result, the distorted ray presented by vector \mathbf{r}_2 with coordinates u_2 and v_2 are given by [49]

$$\mathbf{r}_2 = \begin{bmatrix} u_2 \\ v_2 \end{bmatrix} = \hat{M} \left(\begin{bmatrix} u_1 \\ v_1 \end{bmatrix} - \begin{bmatrix} \rho \\ \phi \end{bmatrix} \right) + \begin{bmatrix} \rho \cos \gamma \\ \phi \end{bmatrix}, \quad (\text{B1})$$

where γ is the angle between the exit ray and the incident ray at the location of the optical element, as shown in Fig. 7. For a crystal, the exit ray angle $\gamma = 2\theta$ after crystal reflection with Bragg's angle θ . For a lens, $\gamma = 0$. Note that the first adjustment of the ray position $-\rho$ is relative to the incident ray. To restore the exit ray to its correct position, it needs to be moved by the amount $\rho \cos \gamma$.

2. Application to the spectrograph case with two-crystal dispersing element

We consider a simplified case, in which only a nonzero angular error ϕ is assumed, while the spatial error $\rho = 0$. Besides, we will trace the trajectory of only the principle ray $\mathbf{r}_1 = 0$, which is initially on the optical axis. In this case Eq. (B1) simplifies to

$$\mathbf{r}_2 = (1 - \hat{M}) \begin{bmatrix} 0 \\ \phi \end{bmatrix} \quad (\text{B2})$$

We recall that ray-transfer matrix of an asymmetrically cut crystal is [32, 50]

$$\hat{C} = \begin{bmatrix} 1/b & 0 \\ 0 & b \end{bmatrix}, \quad (\text{B3})$$

where b is the asymmetry parameter.

In particular, if crystal C_2 is misaligned with an angular error ϕ , the Bragg reflected ray is

$$\begin{aligned} \mathbf{r}_2 &= (1 - \hat{C}_2) \begin{bmatrix} 0 \\ \phi \end{bmatrix} = \begin{bmatrix} 1 - 1/b_2 & 0 \\ 0 & 1 - b_2 \end{bmatrix} \begin{bmatrix} 0 \\ \phi \end{bmatrix} \\ &= \begin{bmatrix} 0 \\ (1 - b_2)\phi \end{bmatrix}. \end{aligned} \quad (\text{B4})$$

This means that the reflected ray propagates at a de-

flexion angle $\Psi_2 = (1 - b_2)\phi$ to the optical axis. In the symmetric case, for which $b_2 = -1$, the deflection angle is $\Psi_2 = 2\phi$. However, if $-b_2 \gg 1$ (as in our experiment) the asymmetrically cut crystal amplifies the deflection angle by a factor $1 - b_2 \gg 1$. At a distance l_3 , the spatial shift from the optical axis is $l_3\Psi_2 = l_3(1 - b_2)\phi$.

If crystal C_1 is misaligned with an angular error ϕ , the ray after two Bragg reflections (neglecting the spacing d_{12}) is

$$\begin{aligned} \mathbf{r}_2 &= \hat{C}_2 (1 - \hat{C}_1) \begin{bmatrix} 0 \\ \phi \end{bmatrix} = \begin{bmatrix} 1/b_2 & 0 \\ 0 & b_2 \end{bmatrix} \begin{bmatrix} 0 \\ (1 - b_1)\phi \end{bmatrix} \\ &= \begin{bmatrix} 0 \\ b_2(1 - b_1)\phi \end{bmatrix}. \end{aligned} \quad (\text{B5})$$

Although $-b_1 \ll 1$, and therefore the angular deflection after the first crystal $(1 - b_1)\phi$ is relatively small, the second crystal still amplifies this deflection to $\Psi_1 = b_2(1 - b_1)\phi$. If $-b_2 \gg 1$, the magnitude of Ψ_1 is close to Ψ_2 , but has the opposite sign. Similarly, the spatial shift from the optical axis at a distance l_3 is $l_3\Psi_1 = l_3(1 - b_1)b_2\phi$.

The analytical calculations provided here are confirmed by numerical simulations with the x-ray optics modeling package Shadow3 [42].

-
- [1] P. Emma, R. Akre, J. Arthur, R. Bionta, C. Bostedt, J. Bozek, A. Brachmann, P. Bucksbaum, R. Coffee, F.-J. Decker, et al., *Nature Photonics* **4**, 641 (2010).
- [2] T. Ishikawa, H. Aoyagi, T. Asaka, Y. Asano, N. Azumi, T. Bizen, H. Ego, K. Fukami, T. Fukui, Y. Furukawa, et al., *Nature Photonics* **6**, 540 (2012).
- [3] H.-S. Kang, C.-K. Min, H. Heo, C. Kim, H. Yang, G. Kim, I. Nam, S. Y. Baek, H.-J. Choi, G. Mun, et al., *Nature Photonics* **11**, 708 (2017).
- [4] W. Decking, S. Abeghyan, P. Abramian, and et al., *Nature Photonics* **14**, 391 (2020).
- [5] C. Bostedt, J. D. Bozek, P. H. Bucksbaum, R. N. Coffee, J. B. Hastings, Z. Huang, R. W. Lee, S. Schorb, J. N. Corlett, P. Denes, et al., *Journal of Physics B: Atomic, Molecular and Optical Physics* **46**, 164003 (2013).
- [6] C. Callegari, A. N. Grum-Grzhimailo, K. L. Ishikawa, K. C. Prince, G. Sansone, and K. Ueda, *Physics Reports* **904**, 1 (2021).
- [7] Yu. Shvyd'ko, R. Röhlberger, O. Kocharovskaya, J. Evers, G. A. Geloni, P. Liu, D. Shu, A. Miceli, B. Stone, W. Hippler, et al., *Nature* **622**, 471 (2023).
- [8] A. M. Kondratenko and E. L. Saldin, *Part. Accel.* **10**, 207 (1980).
- [9] R. Bonifacio, C. Pellegrini, and L. Narducci, *Optics Communications* **50**, 373 (1984), ISSN 0030-4018.
- [10] J. Feldhaus, E. Saldin, J. Schneider, E. Schneidmiller, and M. Yurkov, *Opt. Commun.* **140**, 341 (1997).
- [11] E. Saldin, E. Schneidmiller, Yu. Shvyd'ko, and M. Yurkov, *Nucl. Instrum. Methods Phys. Res. A* **475**, 357 (2001).
- [12] G. Geloni, V. Kocharyan, and E. Saldin, *Journal of Modern Optics* **58**, 1391 (2011).
- [13] J. Amann, W. Berg, V. Blank, F.-J. Decker, Y. Ding, P. Emma, Y. Feng, J. Frisch, D. Fritz, J. Hastings, et al., *Nature Photonics* **6**, 693 (2012).
- [14] I. Inoue, T. Osaka, T. Hara, T. Tanaka, T. Inagaki, T. Fukui, S. Goto, Y. Inubushi, H. Kimura, R. Kinjo, et al., *Nature Photonics* **13**, 1749 (2019).
- [15] I. Nam, C.-K. Min, B. Oh, G. Kim, D. Na, Y. J. Suh, H. Yang, M. H. Cho, C. Kim, M.-J. Kim, et al., *Nature Photonics* **15**, 435 (2021).
- [16] S. Liu, C. Grech, M. Guetg, S. Karabekyan, V. Kocharyan, N. Kujala, C. Lechner, T. Long, N. Mirian, W. Qin, et al., *Nature Photonics* (2023).
- [17] K.-J. Kim, Yu. Shvyd'ko, and S. Reiche, *Phys. Rev. Lett.* **100**, 244802 (2008).
- [18] K.-J. Kim and Yu. V. Shvyd'ko, *Phys. Rev. ST Accel. Beams* **12**, 030703 (2009).
- [19] R. R. Lindberg, K.-J. Kim, Yu. Shvyd'ko, and W. M. Fawley, *Phys. Rev. ST Accel. Beams* **14**, 010701 (2011).
- [20] Z. Huang and R. D. Ruth, *Phys. Rev. Lett.* **96**, 144801 (2006).
- [21] G. Marcus, Y. Ding, J. Duris, Y. Feng, Z. Huang, J. Krzywinski, T. R. T. Maxwell, K.-J. Kim, R. Lindberg, Yu. Shvyd'ko, et al., in *Proceedings of 38th International Free Electron Laser Conference* (Santa Fe, NM, USA, 2017).
- [22] H. P. Freund, P. J. M. van der Slot, and Yu. Shvyd'ko,

- New Journal of Physics **21**, 093028 (2019).
- [23] G. Marcus, A. Halavanau, Z. Huang, J. Krzywinski, J. MacArthur, R. Margraf, T. Raubenheimer, and D. Zhu, *Phys. Rev. Lett.* **125**, 254801 (2020).
- [24] M. Yabashi, J. B. Hastings, M. S. Zolotarev, H. Mimura, H. Yumoto, S. Matsuyama, K. Yamauchi, and T. Ishikawa, *Phys. Rev. Lett.* **97**, 084802 (2006).
- [25] D. Zhu, M. Cammarata, J. M. Feldkamp, D. M. Fritz, J. B. Hastings, S. Lee, H. T. Lemke, A. Robert, J. L. Turner, and Y. Feng, *Appl. Phys. Lett.* **101**, 034103 (2012).
- [26] S. Terentyev, V. Blank, T. Kolodziej, and Yu. Shvyd'ko, *Rev. Sci. Instrum.* **87**, 125117 (2016).
- [27] U. Boesenberg, L. Samoylova, T. Roth, D. Zhu, S. Terentyev, M. Vannoni, Y. Feng, T. B. van Driel, S. Song, V. Blank, et al., *Opt. Express* **25**, 2852 (2017).
- [28] N. Kujala, W. Freund, J. Liu, A. Koch, T. Falk, M. Planas, F. Dietrich, J. Laksman, T. Maltezopoulos, J. Risch, et al., *Rev. Sci. Instrum.* **91**, 103101 (2020).
- [29] Yu. Shvyd'ko, *X-Ray Optics – High-Energy-Resolution Applications*, vol. 98 of *Optical Sciences* (Springer, Berlin Heidelberg, 2004).
- [30] Yu. V. Shvyd'ko, M. Lerche, U. Kuetgens, H. D. Rüter, A. Alatas, and J. Zhao, *Phys. Rev. Lett.* **97**, 235502 (2006).
- [31] V. G. Kohn, A. I. Chumakov, and R. Ruffer, *J. Synchrotron Radiation* **16**, 635 (2009).
- [32] Yu. Shvyd'ko, *Phys. Rev. A* **91**, 053817 (2015).
- [33] Yu. Shvyd'ko, S. Stoupin, K. Mundboth, and J. Kim, *Phys. Rev. A* **87**, 043835 (2013).
- [34] A. I. Chumakov, Yu. Shvyd'ko, I. Sergueev, D. Bessas, and R. Ruffer, *Phys. Rev. Lett.* **123**, 097402 (2019).
- [35] J. Bertinshaw, S. Mayer, F.-U. Dill, H. Suzuki, O. Leupold, A. Jafari, I. Sergueev, M. Spiwek, A. Said, E. Kasman, et al., *Journal of Synchrotron Radiation* **28**, 1184 (2021).
- [36] G. Marcus, J. Anton, L. Assoufid, F.-J. Decker, G. Gassner, K. Goetze, A. Halavanau, J. Hastings, Z. Huang, W. Jansma, et al., in *Proc. FEL'19* (JACoW Publishing, Geneva, Switzerland, 2019), no. 39 in Free Electron Laser Conference, pp. 282–287, ISBN 978-3-95450-210-3, <https://doi.org/10.18429/JACoW-FEL2019-TUD04>, URL <http://jacow.org/fel2019/papers/tud04.pdf>.
- [37] P. Liu, P. Pradhan, A. Miceli, D. A. Walko, D. Shu, J. Sullivan, K. Lang, M. Rivers, M. Balcazar, K. Li, et al., *Phys. Rev. Accel. Beams* **27**, 110701 (2024).
- [38] P. Liu, P. Pradhan, X. Shi, D. Shu, K. Kauchha, Z. Qiao, K. Tamasaku, T. Osaka, D. Zhu, T. Sato, et al., *Journal of Synchrotron Radiation* **31**, 751 (2024).
- [39] A. Macrander, M. Erdmann, N. Kujala, S. Stoupin, S. Marathe, X. Shi, M. Wojcik, D. Nocher, R. Conley, J. Sullivan, et al., in *AIP Conf. Proc.* (2016), vol. 1741, p. 030030.
- [40] B. Lengeler, C. Schroer, J. Tümmler, B. Benner, M. Richwin, A. Snigirev, I. Snigireva, and M. Drakopoulos, *J. Synchrotron Radiation* **6**, 1153 (1999).
- [41] A. Snigirev, V. Kohn, I. Snigireva, and B. Lengeler, *Nature* **384**, 49 (1996).
- [42] M. Sanchez del Río, N. Canestrari, F. Jiang, and F. Cerina, *Journal of Synchrotron Radiation* **18**, 708 (2011).
- [43] L. Rebuffi and M. Sánchez del Río, *Journal of Synchrotron Radiation* **23**, 1357 (2016).
- [44] L. Rebuffi and M. S. del Río, in *Advances in Computational Methods for X-Ray Optics IV*, edited by O. Chubar and K. Sawhney (SPIE, 2017), vol. 10388, p. 28.
- [45] D. Lübbert, T. Baumbach, J. Härtwig, E. Boller, and E. Pernot, *Nucl. Instrum. Methods Phys. Res. B* **160**, 521 (2000).
- [46] S. Stoupin, Yu. Shvyd'ko, E. Trakhtenberg, Z. Liu, K. Lang, X. Huang, M. Wieczorek, E. Kasman, J. Hammonds, A. Macrander, et al., *AIP Conf. Proc.* **1741**, 050020 (2016).
- [47] P. Pradhan, M. Wojcik, X. Huang, E. Kasman, L. Assoufid, J. Anton, D. Shu, S. Terentyev, V. Blank, K.-J. Kim, et al., *Journal of Synchrotron Radiation* **27**, 1553 (2020).
- [48] A. E. Siegman, *Lasers* (University Science Books, Sausalito, California, 1986).
- [49] P. Qi and Yu. Shvyd'ko, *Phys. Rev. Accel. Beams* **25**, 050701 (2022).
- [50] T. Matsushita and U. Kaminaga, *Journal of Applied Crystallography* **13**, 465 (1980).